processes

MDPI

Article

Adaptive Force Control Strategy for Flexible Grasping of Multiple Power Metering Devices Oriented to Power System Operation

Li Wang [1], Chaofan Wang [1,*], Dongyang Zhang [1], Yongxu Xing [1], Linlin Xie [2] and Kun Gao [3,*]

[1] XJ Metering Co., Ltd., Xuchang 461000, China; wangli20081986@163.com (L.W.); zdy45678@163.com (D.Z.); xingyongxu9527@163.com (Y.X.)
[2] XJ Electric Corporation, Xuchang 461000, China; xjbh_xielinlin@163.com
[3] School of Optics and Photonics, Beijing Institute of Technology, Beijing 100081, China
* Correspondence: wangchaofan0203@163.com (C.W.); gaokun@bit.edu.cn (K.G.)

Abstract

As intelligent power grid construction accelerates, power metering warehouses increasingly require fully automatic handling of diverse and fragile devices, ranging from smart meters to current transformers. Conventional rigid clamping schemes apply fixed empirical thresholds and cannot adapt to objects with different sizes, masses, and surface properties, so positioning errors and unexpected collisions often cause component damage. This paper proposes a flexible grasping scheme with adaptive force regulation for power metering equipment. A multifunctional end-effector controller generates gripping force profiles and impedance parameters according to the estimated properties of each target object. An online optimization module based on deep reinforcement learning fuses feedback from a six-axis force sensor and adjusts the grasping trajectory and controller parameters during contact. A closed-loop framework coordinates visual perception before contact with force-controlled execution after contact. Experiments on a UR5e platform with four categories of metering equipment show that the proposed method achieves a grasp success rate of 91.8% and a damage rate of 2.8%, outperforming five comparison methods.

Keywords: compliant grasping; adaptive admittance control; force feedback loop; deep reinforcement learning; power metering equipment

Check for updates

Academic Editors: Alejandro Espinosa Calderón and Horacio Rostro-Gonzalez

Received: 21 June 2026
Revised: 22 July 2026
Accepted: 25 July 2026
Published: 5 August 2026

Copyright: © 2026 by the authors. Licensee MDPI, Basel, Switzerland. This article is an open access article distributed under the terms and conditions of the Creative Commons Attribution (CC BY) license.

1. Introduction

The accelerated deployment of smart grid infrastructure has created an urgent demand for automated operations within power metering warehouses [1]. Throughput requirements continue to rise, and the range of equipment to be handled keeps expanding. Smart meters, communication modules, and instrument transformers represent typical categories [2]. These items exhibit diverse physical specifications, and their material structures are often fragile [3]. Conventional rigid grasping strategies rely on preprogrammed trajectories. They apply fixed gripping forces regardless of object identity [4]. Such approaches struggle to accommodate physical variations across multi-specification objects [5].

Position uncertainties during bin picking present severe challenges. Objects rest in unstructured piles. Unexpected contacts between the end-effector and equipment surfaces induce mechanical shocks [6]. These shocks risk permanent damage to delicate internal circuits. Operational safety is simultaneously compromised [7]. Developing intelligent robotic grasping systems tailored for fragile power metering equipment has emerged as

a critical challenge [8]. Researchers have investigated automated storage and retrieval systems for electrical components. Yet specialized solutions for heterogeneous fragile items remain scarce [9]. Early work in robotic grasping concentrated on analytical grasp synthesis. Geometric contact analysis dominated research for rigid mechanical parts [10].

Recent advances leverage deep learning for visual grasp detection. Six-degree-of-freedom pose estimation has achieved high accuracy [11]. Convolutional neural networks and point cloud processing pipelines enable robots to predict stable grasp configurations from RGB-D sensor data [12]. These vision-centric methods excel in structured settings. Object geometries must be well defined. Surface properties should remain homogeneous [13]. However, they predominantly target rigid objects. Uniform material characteristics are implicitly assumed [14]. The underlying algorithms rely on empirical force thresholds. These thresholds are derived from limited object categories [15]. When confronted with fragile or compliant items, fixed thresholds prove inadequate [16]. The absence of material-aware adaptation produces two failure modes. Excessive gripping forces crush delicate housings. Insufficient forces cause slippage during transport [17]. Both outcomes generate economic losses and safety hazards. Compliant manipulation offers a promising alternative to rigid grasping paradigms [18]. Admittance control has been extensively studied for regulating contact interactions. Admittance control provides complementary benefits for robotic manipulators in external environments [19]. These methods establish dynamic relationships between end-effector position and contact force. Virtual mass–spring–damper models capture this coupling [20].

By modulating stiffness and damping parameters, robots achieve safer contact behavior [21]. Admittance control decouples force tracking from position control. External disturbances are handled more intuitively [22]. Hybrid force–position control strategies regulate certain degrees of freedom in position. Other degrees of freedom modulate force simultaneously [23]. Despite these theoretical advances, most compliant control implementations employ fixed impedance parameters. These parameters remain constant throughout the entire grasping cycle. Such constancy cannot reconcile competing requirements. Grasping stability and operational safety demand different settings across objects with divergent mass, stiffness, and surface friction properties.

Force feedback constitutes another essential component in delicate object manipulation. Six-axis force–torque sensors installed at the wrist provide real-time measurements of contact wrench [24]. Fingertip sensors offer additional spatial resolution. These measurements enable online detection of collision events. Slippage onset is identified before object drop occurs. Researchers have integrated force signals into grasp stability criteria. Grip force modulation laws have been established accordingly. Tactile sensing arrays offer distributed pressure profiles. Local contact geometry is revealed. Material compliance is estimated from these readings. Nevertheless, most existing force-based systems operate through predefined reactive rules. Proportional–integral–derivative controllers with constant gains remain prevalent. The mapping from raw sensor readings to control adjustments is largely handcrafted. Rule-based architectures lack generalization capacity [25]. Novel object categories require manual redesign. Force profiles cannot be optimized automatically for heterogeneous equipment sets. Furthermore, sensor processing introduces latency. Discrete control loops compound this delay. Timely compensation for rapid contact transients is often impossible.

To address the aforementioned challenges, this paper proposes a multi-object compliant grasping and adaptive force control method for power metering equipment. The contributions of this work are as follows.

(1) A multifunctional end-effector controller is designed for compliant grasping of heterogeneous metering equipment. The controller estimates object properties through

confidence-weighted fusion of visual measurements and database records, and maps these properties to target gripping forces and impedance parameters through an exponential stiffness adaptation law. This property-to-parameter mapping removes the manual tuning required by fixed-impedance schemes.

(2) A safety-constrained online optimization mechanism based on deep reinforcement learning is constructed. Every policy output passes through a projection layer that enforces positive definiteness and bounds on the controller parameters, and a hard override bypasses the policy when the crushing limit is approached. The learning-based correction therefore coexists with explicit bounds on the controller parameters that hold independently of the policy output.

(3) A closed-loop framework integrating visual perception and force-controlled execution is established. An asynchronous fusion scheme coordinates the visual stream and the force loop, and contact-triggered switching with continuity constraints ensures smooth transitions between the two modalities.

The remainder of this paper is organized as follows. Section 2 presents the overall system architecture and details the design of the multifunctional end-effector controller. Section 3 develops the deep-reinforcement-learning-based online optimization mechanism for adaptive admittance control. Section 4 establishes the closed-loop control framework that integrates visual perception with force-controlled execution. Section 5 reports the experimental setup and results. Section 6 concludes this paper and discusses future research directions.

2. Multifunctional End-Effector Controller Design

2.1. System Architecture and Mechanical Configuration

The multifunctional end-effector serves as the primary physical interface between the robotic manipulator and power metering equipment. Its mechanical configuration integrates a parallel jaw gripper, a six-axis force–torque sensor, and a proximity vision module within a unified housing. This integration enables simultaneous force measurement and visual inspection throughout the grasping sequence. The overall architecture of the multifunctional end effector controller is shown in the following Figure 1.

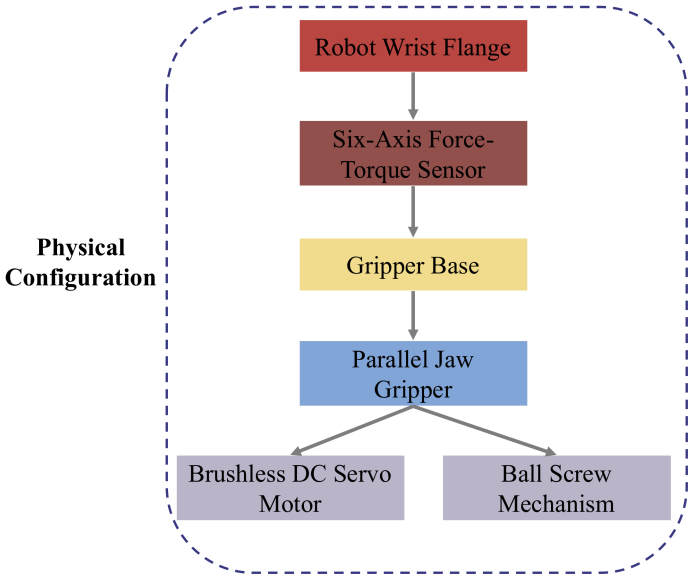


Figure 1. Overall architecture of the multifunctional end-effector controller.

The gripper mechanism employs a parallel jaw structure driven by a brushless DC servo motor [4], which provides symmetric force distribution during closure and remains suitable for fine grasping of small communication modules. The transmission system utilizes a ball screw mechanism. This component converts rotary motion into linear displacement with minimal backlash. Position repeatability reaches ±0.02 mm. Such precision proves essential for aligning with objects in cluttered bins.

This paper employs interchangeable fingertip pads fabricated from silicone rubber with Shore hardness 40A [6]. The pads attach to aluminum finger bases through magnetic couplings. The soft polymer distributes contact pressure across a finite area. Stress concentrations that typically develop at point contacts are thereby eliminated. The contact area increases with grip force.

The six-axis force–torque sensor mounts between the gripper base and the robot wrist flange [6]. This placement measures interaction wrenches at the grasp point. Sensor resolution reaches 0.1 N in force and 0.005 Nm in torque. The sampling rate operates at 1 kHz. This bandwidth captures rapid contact transients that occur during bin picking. A signal conditioning module performs real-time filtering. A second-order low-pass filter with cutoff frequency at 100 Hz suppresses high-frequency noise without introducing excessive phase lag. Since the wrist sensor measures the external interaction wrench rather than the internal clamping force, the gripping force between the jaws is estimated from the servo motor current through a calibrated current–force model. Gravity and inertial wrenches induced by the gripper and the grasped object are compensated online before the force signals enter the controller.

The proximity vision module consists of a compact RGB-D camera mounted on the gripper frame [9]. This placement provides a local view of the target object. Global camera configurations suffer from occlusion by the gripper body. The depth stream guides initial approach trajectory planning. The color stream supports object classification. Visual and force modalities complement each other. Vision provides global pose estimates before contact. Force provides local interaction details after contact. The hierarchical controller architecture is shown in the following Figure 2.

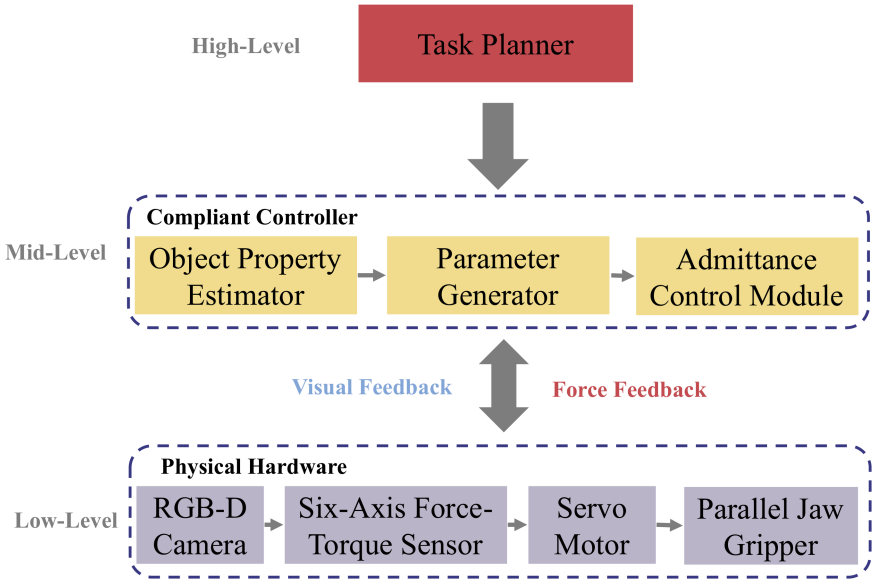


Figure 2. Hierarchical controller architecture.

The controller architecture follows a hierarchical organization. The high-level task planner coordinates the overall grasping sequence. It receives warehouse management system commands and selects target objects from the current bin. The mid-level compliant

controller generates target force and impedance parameters. This module implements the algorithms described in Section 2.2. The low-level servo driver executes motor current commands. This layered structure isolates safety-critical contact regulation from high-level decision logic. Failures in the task planner do not compromise contact stability. The low-level loop maintains safe behavior independently.

2.2. Compliant Grasping Algorithm and Adaptive Parameter Generation

Fixed-impedance settings cannot reconcile grasping stability with operational safety when objects differ greatly in mass and stiffness [26]. The proposed algorithm addresses this limitation through systematic parameter adaptation in three sequential stages. First, object properties are estimated from visual and tactile cues. Second, target gripping forces and impedance parameters are generated based on these estimates. Third, the admittance controller tracks these targets during physical interaction.

Throughout this paper, the low-level controller is referred to as an admittance controller, because it takes the measured contact force as input and produces the motion correction as output. The term impedance is used only to describe the virtual mass–damper–spring parameters that shape the desired interaction dynamics, following the common usage in compliant manipulation research.

The foundation rests upon an admittance control model. The desired dynamic relationship between external force and position deviation follows a virtual mass–spring–damper system [6]. The governing equation in Cartesian space is expressed as

$$M_d\ddot{e}(t) + D_d\dot{e}(t) + K_d e(t) = F_{ext}(t) - F_{ref}(t) \quad (1)$$

where $e(t) = x(t) - x_d(t)$ represents the position error vector. $x(t)$ denotes the actual end-effector position. $x_d(t)$ denotes the desired trajectory generated by the motion planner. M_d, D_d, and K_d denote the virtual mass, damping, and stiffness matrices, respectively. These matrices are diagonal and positive definite. $F_{ext}(t)$ denotes the measured external wrench vector. $F_{ref}(t)$ denotes the reference contact force vector. This formulation decouples force tracking from position control. External disturbances propagate through the admittance filter rather than directly into the position servo. The resulting motion exhibits inherently compliant behavior. Contact forces remain bounded even for stiff environments. This paper selects admittance control for the end-effector regulation.

The object property estimation module processes multimodal inputs. Visual features provide geometric and material cues. The equipment database provides nominal specifications. Let m_v denote the mass estimated from the object volume extracted from RGB-D data and the nominal material density retrieved from the equipment database. Let m_d denote the nominal mass retrieved from the warehouse database. The estimated mass $\hat{m}$ is computed through confidence-weighted fusion:

$$\hat{m} = c_m m_v + (1 - c_m) m_d \quad (2)$$

where c_m represents the visual confidence coefficient ranging from zero to one. This coefficient reflects the reliability of visual measurement under current illumination and occlusion conditions. The coefficient c_m is computed online from the occlusion ratio and the segmented point count. It adapts automatically to the sensing conditions instead of being manually assigned. When the camera view is unobstructed, c_m approaches one. When heavy occlusion occurs, the system relies primarily on database entries. Similarly, let k_v

denote the stiffness estimated from visual material classification. Let k_d denote the nominal stiffness from the database. The estimated stiffness $\hat{k}$ follows:

$$\hat{k} = c_k k_v + (1 - c_k) k_d \tag{3}$$

where c_k represents the corresponding confidence coefficient. The coefficient c_k is computed in the same manner as c_m. This fusion strategy ensures robust estimation even with partial sensory information.

The target grip force must prevent slippage while avoiding material damage [9]. The minimum required force follows the Coulomb friction model. The expression reads

$$F_{g,min} = \frac{\hat{m} g}{\mu_s n_f} \tag{4}$$

where g denotes gravitational acceleration. μ_s denotes the static friction coefficient between the fingertip material and the object surface. This coefficient is determined experimentally for each material pairing. It was measured through inclined-plane tests for each fingertip-material pairing. n_f denotes the number of contact fingers. For the parallel jaw gripper, $n_f = 2$. This value establishes the lower bound for safe grasping. Forces below this threshold guarantee slippage under static conditions.

Dynamic effects during transport require additional grip force. Acceleration and deceleration generate inertial loads. The reference grip force incorporates a dynamic compensation term:

$$F_{ref} = F_{g,min} + k_a \hat{m} a_{max} \tag{5}$$

The dynamic load factor k_a is set to 1.2, which corresponds to the acceleration limit a_{max} in the motion planner.

Material safety imposes an upper bound on the allowable grip force [12]. Excessive force crushes delicate housings. The crushing limit is defined as

$$F_{lim} = \hat{k} \delta_{max} \tag{6}$$

where δ_{max} denotes the maximum permissible deformation of the object surface. This limit is specified for each equipment category in the database. This limit is derived from the linear stiffness model. The controller verifies that $F_{ref} \leq F_{lim}$ before executing the grasp. If this constraint is violated, the system reduces the planned acceleration or selects an alternative grasp configuration.

The virtual stiffness matrix adapts to object properties. Excessive stiffness generates large contact forces upon impact. Such forces crush delicate housings. Insufficient stiffness compromises positioning accuracy. The robot cannot maintain stable contact. The diagonal elements of K_d are tuned according to an exponential decay model:

$$K_{d,i} = K_{0,i} \exp\left(-\alpha_i \frac{\hat{k}}{k_{\text{nom}}} + \beta_i \frac{\hat{m}}{m_{\text{nom}}} \right) \tag{7}$$

where $K_{0,i}$ denotes the baseline stiffness for the i-th degree of freedom. α_i denotes the stiffness decay rate with respect to object rigidity. Highly rigid objects cause rapid stiffness reduction. This behavior limits impact forces. β_i denotes the mass compensation gain. Heavier objects receive increased stiffness to prevent sagging during transport. The baseline stiffness $K_{0,i}$ is set to 2500 N/m for the translational axes and 60 Nm/rad for the rotational axes, which lies within the stable control bandwidth of the UR5e manipulator. The decay rate α_i and the mass compensation gain β_i were selected by a grid search over candidate

values on a validation set of retired metering devices, using the grasp success rate and the damage rate as the criteria.

The virtual damping matrix ensures stable transient behavior. The diagonal elements follow the critical damping relationship:

$$D_{d,i} = 2\xi_i\sqrt{M_{d,i}K_{d,i}} \tag{8}$$

where ξ_i denotes the damping ratio. Oscillatory contact behavior is thereby prevented. The damping ratio is set to 0.7, slightly below critical damping, which suppresses oscillatory contact behavior without making the response sluggish.

The energy dissipation rate during contact serves as a stability indicator. The time derivative of the Lyapunov function candidate must remain non-positive to guarantee passive contact behavior. The candidate function is defined as $V = 1/2\left(\dot{e}^T M_d \dot{e} + e^T K_d e\right)$. Its derivative satisfies

$$\dot{V} = \dot{e}^T(F_{ext} - F_{ref}) - \dot{e}^T D_d \dot{e} \leq 0 \tag{9}$$

The force profile generator produces smooth force references to avoid step changes. A sigmoid transition function modulates the reference from initial to target value:

$$F_{ref}(t) = F_{init} + (F_{target} - F_{init}) \cdot \frac{1}{1 + \exp(-\tau(t - t_0))} \tag{10}$$

where F_{init} denotes the initial contact force measured at first touch. F_{target} denotes the steady-state target. τ denotes the transition rate controlling activation speed. t_0 denotes the transition midpoint. This smooth activation prevents mechanical shock at contact onset.

3. Online Optimization Mechanism Based on Deep Reinforcement Learning

3.1. Markov Decision Process Formulation for Contact Tasks

The compliant grasping algorithm in Section 2 generates baseline impedance parameters and force profiles. These parameters provide reasonable initial settings. However, they cannot anticipate all contact transients during physical interaction. Unmodeled surface irregularities and dynamic disturbances require online corrections. This paper formulates the contact regulation task as a Markov Decision Process. This formulation enables sequential decision-making under uncertainty.

The process is defined by the tuple $\mathcal{M} = \{\mathcal{S}, \mathcal{A}, \mathcal{P}, \mathcal{R}, \gamma\}$. $\mathcal{S}$ represents the continuous state space. $\mathcal{A}$ represents the continuous action space. $\mathcal{P}$ denotes the state transition probability. $\mathcal{R}$ denotes the reward function. γ denotes the discount factor. This standard definition provides the mathematical foundation for policy optimization.

The state vector s_t at time step t aggregates multimodal sensory information. It comprises four distinct components. The first component encodes visual features. A pretrained convolutional neural network extracts a feature vector f_v from the RGB-D image. This vector captures object geometry and local surface orientation. The second component encodes force–torque readings. A sliding window of the most recent ten samples from the six-axis sensor forms a vector f_f. This temporal window captures force transients and oscillation patterns. The third component encodes current impedance settings. The diagonal elements of K_d and D_d are stacked into a 12-dimensional vector f_i. These values reflect the controller configuration established in Section 2. The fourth component encodes

task progress. The position error e_p and force deviation e_f constitute a vector f_e. The complete state vector is expressed as

$$s_t = \left[f_v^\top, f_f^\top, f_i^\top, f_e^\top \right]^\top \tag{11}$$

This high-dimensional space necessitates function approximation. Deep neural networks provide the required representational capacity [27]. The action vector a_t specifies incremental adjustments to the control targets. The policy network outputs corrections to both the target pose and the virtual admittance parameters. The action is defined as

$$a_t = \left[\Delta x_d^\top, \Delta K_d^\top, \Delta D_d^\top \right]^\top \tag{12}$$

where Δx_d denotes the incremental correction to the desired position trajectory. ΔK_d and ΔD_d denote the incremental corrections to the virtual stiffness and damping matrices. These increments are added to the baseline values generated by the algorithm in Section 2. The resulting sum passes through a projection layer. This layer enforces positive definiteness and bounds. Such constraints maintain controller stability. The robot executes action a_t. The physical system evolves according to contact mechanics. The next state s_{t+1} is sampled from the conditional distribution

$$s_{t+1} \sim \mathcal{P}(s_{t+1} | s_t, a_t). \tag{13}$$

The reward function shapes the desired contact behavior. It combines four objectives. The first objective penalizes force tracking errors. Large deviations between measured and reference forces indicate poor contact regulation. The second objective penalizes excessive contact instability. Oscillatory force patterns indicate underdamped behavior. The third objective penalizes safety violations. Contact forces approaching the crushing limit F_{lim} indicate imminent damage. The fourth objective rewards task progress. Reduction in position error indicates successful approach to the target grasp configuration [14]. The scalar reward at time t is computed as

$$r_t = -w_1 \| F_{ext} - F_{ref} \|^2 - w_2 \sigma_F^2 - w_3 \max(0, F_{max} - F_{safe}) - w_4 \| e_p \|^2 \tag{14}$$

where w_1 through w_4 denote positive weighting coefficients. σ_F denotes the standard deviation of the force magnitude over the recent window. F_{max} denotes the peak measured force. F_{safe} denotes a safety threshold set below F_{lim} with a 20 percent margin. Among the four objectives, the safety-violation term is assigned the largest weight. The discounted return from time step t is defined as

$$G_t = \sum_{k=0}^{\infty} \gamma^k r_{t+k} \tag{15}$$

where γ is set to 0.99. This high discount factor prioritizes long-term safety over immediate reward maximization.

3.2. Multimodal Policy Network and Training Algorithm

This paper employs the Proximal Policy Optimization algorithm. This algorithm offers stable training and sample efficiency. These properties prove essential for robot learning.

The policy network π_θ processes the multimodal state vector. It employs three parallel encoder branches. The visual branch processes f_v through two fully connected layers. The force branch processes f_f through a one-dimensional convolutional layer followed by a long short-term memory layer. This architecture captures temporal dependencies in the

force sequence. The impedance branch processes f_i through two fully connected layers. The encoded representations from all three branches are concatenated. This fused vector passes through two shared fully connected layers. The final layer splits into two heads. The policy head outputs the mean $\mu_\theta(s)$ and diagonal covariance $\Sigma_\theta(s)$ of a multivariate Gaussian distribution. The value head outputs a scalar estimate $V_\phi(s)$. The stochastic policy is expressed as

$$a_t \sim \pi_\theta(a_t|s_t) = \mathcal{N}(\mu_\theta(s_t), \Sigma_\theta(s_t)) \tag{16}$$

where θ denotes the policy network parameters. ϕ denotes the value network parameters. These parameters are updated jointly during training. The state-value function estimates the expected return from a given state. It is defined as

$$V_\phi(s) = \mathbb{E}_{\pi_\theta}[G_t|s_t = s] \tag{17}$$

This estimate serves two purposes. It reduces variance in the policy gradient. It provides the baseline for advantage estimation [14]. The advantage function measures the relative value of a specific action. It quantifies how much better a_t performs compared to the average action at state s_t. The advantage is approximated as

$$\hat{A}_t = G_t - V_\phi(s_t) \tag{18}$$

This temporal-difference residual provides a low-variance signal for policy improvement. Actions yielding positive advantages are reinforced. Actions yielding negative advantages are suppressed. The probability ratio between the current policy and the old policy is defined as

$$r_t(\theta) = \frac{\pi_\theta(a_t|s_t)}{\pi_{\theta_{old}}(a_t|s_t)} \tag{19}$$

This ratio measures the relative probability of the taken action under the updated policy. The PPO clipped surrogate objective limits the effective change:

$$L^{CLIP}(\theta) = \mathbb{E}_t\left[\min\left(r_t(\theta)\hat{A}_t, \text{clip}(r_t(\theta), 1-\epsilon, 1+\epsilon)\hat{A}_t\right)\right] \tag{20}$$

where ϵ denotes the clipping hyperparameter set to 0.2. The minimum operator selects the more conservative of the two terms. When the advantage is positive and the ratio exceeds $1 + \epsilon$, the clipped term becomes constant. Further increase in action probability receives no additional reward. This mechanism prevents excessive policy updates. Training stability improves significantly. The value network is trained to minimize the squared error between predicted and actual returns. The value loss is

$$L^{VF}(\phi) = \mathbb{E}_t\left[\left(V_\phi(s_t) - G_t\right)^2\right] \tag{21}$$

An entropy bonus encourages exploration. It prevents premature convergence to deterministic policies. The entropy term is

$$L^{ENT}(\theta) = \mathbb{E}_t[-\log \pi_\theta(a_t|s_t)] \tag{22}$$

The total loss function combines these three terms with weighting coefficients c_1 and c_2:

$$L(\theta, \phi) = -L^{CLIP}(\theta) + c_1 L^{VF}(\phi) - c_2 L^{ENT}(\theta) \tag{23}$$

The c_1 and c_2 balance policy improvement, value accuracy, and exploratory behavior. The generalized advantage estimator further reduces variance in the advantage compu-

tation. It introduces a parameter λ that interpolates between low-bias and low-variance estimates. The advantage is computed recursively as

$$\hat{A}_t = \delta_t + (\gamma\lambda)\hat{A}_{t+1} \tag{24}$$

where $\delta_t = r_t + \gamma V_\phi(s_{t+1}) - V_\phi(s_t)$ denotes the temporal-difference error. This configuration prioritizes bias reduction while maintaining acceptable variance.

Training proceeds through iterative data collection and policy updates. The robot interacts with the environment for a fixed number of time steps per episode. Episode termination occurs upon successful grasping, safety violation, or timeout. Collected trajectories are stored in a replay buffer. The PPO update performs five epochs of minibatch gradient descent over this buffer.

3.3. Real-Time Deployment and Safety-Constrained Optimization

The trained policy deploys on the physical robot for online trajectory adjustment. This section describes the inference pipeline and safety mechanisms. These components ensure stable real-time operation. The control system operates with hierarchical rates. The low-level admittance filter and the servo loop run at 1 kHz on the real-time controller, which is a standard configuration for industrial manipulators. At each control cycle, the system acquires the current sensor readings. The raw action a_t specifies relative adjustments. These adjustments are mapped to absolute controller commands. The updated desired position and impedance parameters are computed as

$$x_d^{new} = x_d^{base} + \Delta x_d \tag{25}$$

$$K_d^{new} = \mathrm{Proj}_{\mathcal{K}}(K_d^{base} + \Delta K_d) \tag{26}$$

$$D_d^{new} = \mathrm{Proj}_{\mathcal{D}}(D_d^{base} + \Delta D_d) \tag{27}$$

where x_d^{base}, K_d^{base}, and D_d^{base} denote the baseline values from Section 2. $\mathrm{Proj}_{\mathcal{K}}$ and $\mathrm{Proj}_{\mathcal{D}}$ denote projection operators. These operators enforce lower and upper bounds on the diagonal elements. They also ensure that K_d and D_d remain positive definite. The projection prevents unstable controller configurations that might emerge from out-of-distribution states.

The action smoothing module reduces high-frequency jitter [15]. Raw network outputs occasionally exhibit rapid oscillations. Such oscillations excite unmodeled structural vibrations. An exponential moving average filters the action sequence:

$$\bar{a}_t = \eta a_t + (1-\eta)\bar{a}_{t-1} \tag{28}$$

where η denotes the smoothing coefficient. This filter preserves the low-frequency trend of the policy. It suppresses noise that might destabilize the mechanical system.

The safety override mechanism monitors critical conditions. If the measured force exceeds F_{lim} at any instant, the RL policy is bypassed. The system switches to a conservative emergency mode. In this mode, the gripper opens immediately. The robot retreats along the approach direction. This hard constraint guarantees that the learning-based system never violates physical safety limits.

4. Closed-Loop Control Framework Integrating Visual Perception and Force-Controlled Execution

4.1. Framework Architecture and Perception–Action Coupling

The framework integrates visual perception and force-controlled execution through a hierarchical coordination structure. This structure manages information flow across

three functional layers. The visual perception layer extracts global object properties. The force-controlled execution layer regulates local contact dynamics. The coordination layer fuses these modalities and manages phase transitions.

The visual perception layer processes data from the gripper-mounted camera described in Section 2. A point cloud segmentation algorithm extracts the target object surface. Principal component analysis determines the principal axes. The object centroid and orientation define a six-dimensional pose vector x_{obj}^{cam} in the camera frame. This vector transforms into the robot base frame through the calibrated hand–eye transformation:

$$\hat{x}_{obj}^{base} = T_{base}^{cam} x_{obj}^{cam} \tag{29}$$

where $T_{base}^{cam} \in SE(3)$ denotes the homogeneous transformation matrix. This matrix is calibrated offline using a standard ArUco board procedure. Visual estimation carries inherent uncertainty. Depth sensor noise increases with distance. Object occlusion reduces point cloud completeness. This uncertainty is quantified through a diagonal covariance matrix:

$$\Sigma_{vis} = \mathrm{diag}(\sigma_x^2, \sigma_y^2, \sigma_z^2, \sigma_{rx}^2, \sigma_{ry}^2, \sigma_{rz}^2) \tag{30}$$

where each diagonal element reflects the estimated variance along the corresponding degree of freedom. These values are derived from the point cloud density distribution and the camera intrinsic noise model.

The coordination layer assigns fusion weights based on visual reliability. When visual confidence is high and contact has not occurred, the system trusts visual pose estimates. When contact forces rise or visual occlusion degrades quality, the system shifts trust toward proprioceptive feedback. The visual confidence coefficient is computed as:

$$c_{vis} = \exp\left(-\frac{d_{occ}^2}{2\sigma_{occ}^2}\right) \cdot \frac{N_{pts}}{N_{pts} + N_{min}} \tag{31}$$

where d_{occ} denotes the occlusion depth measured from the missing depth pixels. σ_{occ} denotes the decay parameter controlling sensitivity to occlusion. N_{pts} denotes the segmented point count. N_{min} denotes the minimum required points for reliable estimation. The first term penalizes heavy occlusion. The second term penalizes sparse point clouds. The fused target pose combines the visual estimate with the current end-effector pose:

$$\hat{x}_{target} = c_{vis}\hat{x}_{obj}^{base} + (1 - c_{vis})x_{ee} \tag{32}$$

where x_{ee} denotes the current end-effector pose measured by the robot joint encoders. This weighted combination ensures smooth transitions when visual data becomes unreliable. The robot does not execute abrupt motions toward erroneous visual targets. The commanded velocity follows a proportional–derivative law:

$$v_{cmd} = K_{p,vis}(\hat{x}_{target} - x_{ee}) - K_{d,vis}\dot{x}_{ee} \tag{33}$$

where $K_{p,vis}$ and $K_{d,vis}$ denote the visual servo gains. These gains are tuned for rapid convergence without overshoot. Overshoot risks premature contact with neighboring objects in cluttered bins.

Contact detection triggers the transition from visual tracking to force-controlled execution [17]. A binary contact indicator is defined:

$$\mathcal{H}(t) = \begin{cases} 1 & \|F_{ext}(t)\| > F_{th} \\ 0 & \text{otherwise} \end{cases} \tag{34}$$

where F_{th} denotes the force threshold. This threshold is set above the sensor noise floor yet below the minimum expected contact force. This threshold is set to 0.5 N, which is well above the sensor noise floor of ± 0.1 N and below the minimum gripping force of 1.25 N required by the lightest object.

4.2. Coordinated Execution and Closed-Loop Stability

Upon contact detection, the framework switches primary control authority from the visual servo to the admittance controller. The visual perception layer continues operating in the background. It provides global monitoring and detects object displacement during manipulation. The force-controlled execution layer activates the algorithms from Sections 2 and 3.

The reference trajectory for the admittance controller is initialized at the contact instant. Let t_c denote the contact time. The initial reference equals the end-effector pose at that instant:

$$x_d(t_c) = x_{ee}(t_c) \tag{35}$$

The RL policy from Section 3 further modulates the impedance parameters and injects corrective offsets. The complete reference is expressed as:

$$x_d(t) = x_{ee}(t_c) + \int_{t_c}^{t} \dot{e}_{adm}(\tau) d\tau + \Delta x_{rl}(t) \tag{36}$$

where $\dot{e}_{adm}$ denotes the velocity output from the admittance filter. $\Delta x_{rl}(t)$ denotes the incremental pose correction from the RL policy network. This formulation ensures continuity at the switching instant. Jerky transitions that might destabilize contact are avoided.

The closed-loop error incorporates both force tracking and visual estimation inaccuracies. Let $e(t) = x_{ee}(t) - x_d(t)$ denote the tracking error relative to the reference trajectory $x_d(t)$. Let $\delta_{vis}(t) = K_d[\hat{x}_{obj}^{base}(t) - x_{true}(t)]$ denote the equivalent disturbance induced by visual estimation inaccuracy [21]. The extended admittance dynamics become:

$$M_d\ddot{e} + D_d\dot{e} + K_d e = F_{ext} - F_{ref} + \delta_{vis}(t) \tag{37}$$

This expression assumes quasi-static visual error evolution. The disturbance term represents the stiffness reaction against target misalignment. When visual estimation is precise, this term vanishes. When occlusion or reflection corrupts the RGB-D stream, this term introduces a bounded perturbation.

Stability of the combined visual–force loop is analyzed through an augmented Lyapunov function. This function combines mechanical energy with the visual disturbance bound:

$$V_{cl} = \frac{1}{2}\dot{e}^T M_d \dot{e} + \frac{1}{2} e^T K_d e + \frac{1}{2\rho}\|\delta_{vis}\|^2 \tag{38}$$

where ρ denotes a positive weighting constant. This constant balances the contribution of visual uncertainty against mechanical state errors [22]. The time derivative along the system trajectories satisfies:

$$\dot{V}_{cl} \leq -\lambda_{\min}(D_d)\|\dot{e}\|^2 + \lambda_{\max}(K_d)\|\dot{e}\|\|\delta_{vis}\| + \frac{\beta}{\gamma}\|\delta_{vis}\|^2 \tag{39}$$

where λ_{min} and λ_{max} denote the minimum and maximum eigenvalues of the corresponding matrices. By selecting D_d sufficiently large and γ appropriately, the negative definite terms

dominate. The system remains ultimately bounded. The error converges to a compact set proportional to the visual uncertainty. The practical stability condition requires:

$$\lambda_{\min}(D_d) > \frac{\lambda_{\max^2}(K_d)}{4\epsilon} \tag{40}$$

The stability result holds under the following boundary conditions. The projection layer confines each translational stiffness element to the interval [500, 4000] N/m and keeps the damping elements within the corresponding near-critical range computed from. The pose correction injected by the policy is limited to 5 mm per control cycle. The visual disturbance is bounded by the worst-case value derived from the estimation covariance. Under these conditions, the negative definite terms dominate the disturbance terms, and the closed-loop error remains ultimately bounded within a compact set whose size is proportional to the visual uncertainty [28].

The coordination layer handles asynchronous sensory streams. The vision system updates at 30 Hz. The state vector for the RL policy assembles these heterogeneous rates through zero-order hold:

$$s_t = \left[f_v(t_k)^\top, f_f(t)^\top, f_i(t)^\top, f_e(t)^\top\right]^\top,\ t_k \le t < t_{k+1} \tag{41}$$

where t_k denotes the most recent visual frame timestamp. The visual feature f_v remains constant between frames. The force feature f_f updates at every control cycle.

5. Experimental Results and Analysis

To validate the proposed method, this paper establishes a comprehensive evaluation protocol on a UR5e robotic platform. A six-axis force–torque sensor and a proximity RGB-D camera are integrated within the gripper housing. Four categories of power metering equipment are selected for testing. These categories represent the typical physical diversity encountered in actual warehouses. The dataset comprises single-phase smart meters, three-phase smart meters, communication modules and low-voltage current transformers. Table 1 summarizes the physical properties of the test objects. In each trial, three to five objects were placed in the bin in unstructured piles with random poses, and partial occlusion among objects was common. The force–torque sensor exhibits a noise floor of approximately $\pm$0.1 N after the 100 Hz low-pass filtering, and the contact detection threshold was set to 0.5 N, well above this floor and below the minimum gripping force required by the lightest object. All learning-based components were trained on a workstation equipped with a single NVIDIA RTX 4060 GPU with 8 GB of video memory. The policy was trained directly on the robotic platform using retired and scrapped metering devices provided by the warehouse, so that the exploration process did not consume intact inventory. Training lasted for 2000 episodes, and the moving-average return had already plateaued at approximately 1600 episodes. The accumulated interaction time was approximately 24 h distributed over five working days. The learning rate was set to 3×10^{-4}.

Table 1. Physical feature of the test objects.

Category	Primary Material	Mass (kg)
Single-phase smart meter	ABS plastic	0.82
Three-phase smart meter	Plastic–metal hybrid	1.48
Communication module	PCB with plastic enclosure	0.14
LV current transformer	Resin-coated copper	2.18

To verify the advantages of the method proposed in this paper, five methods were selected for comparison. The results are shown in Table 2. The first baseline is a fixed admittance controller with empirically tuned parameters. This method represents conventional rigid grasping strategies. The second baseline adopts Bayesian optimization for robust grasping. This approach is denoted as BOG [2]. The third baseline employs reinforcement learning grasping with force feedback from compliant fingers, abbreviated as RL-FF [12]. The fourth baseline implements adaptive force control based on vision demonstration, termed AFC [14]. The fifth baseline utilizes a diffusion policy guided by vision and force observations, denoted as DPVF [21]. The proposed method is evaluated alongside these counterparts under identical physical conditions. The performance of each method is as follows. Grasp success rate measures the percentage of trials where the object is lifted and transported to the target zone without drop. Damage rate records the percentage of trials resulting in drop or visible surface deformation.

Table 2. Overall grasp success rate and damage rate.

Category	Success Rate (%)	Damage Rate (%)
Fixed IC	71.6 ± 6.3	8.4 ± 3.1
BOG [2]	80.4 ± 5.2	6.6 ± 2.5
RL-FF [12]	83.6 ± 4.5	5.8 ± 2.3
AFC [14]	85.2 ± 3.8	4.5 ± 2.1
DPVF [21]	87.5 ± 4.1	4.2 ± 1.8
Proposed	91.8 ± 3.2	2.8 ± 1.4

The fixed admittance controller achieves the lowest success rate at 71.6%, with a damage rate of 8.4%, because its constant parameters cannot accommodate the mass variation from 0.14 kg to 2.18 kg. The Bayesian optimization process requires multiple exploration steps. This delay occasionally misses the optimal grasping window in cluttered bins. The damage rate remains relatively high at 6.6%. The proposed method attains 91.8% success with a 2.8% damage rate. The integration of visual perception and force-controlled execution enables preemptive pose correction. The RL-based online optimization further refines the impedance parameters during contact. The following Figure 3 illustrates the force tracking behavior during a representative grasping trial on the three-phase smart meter.

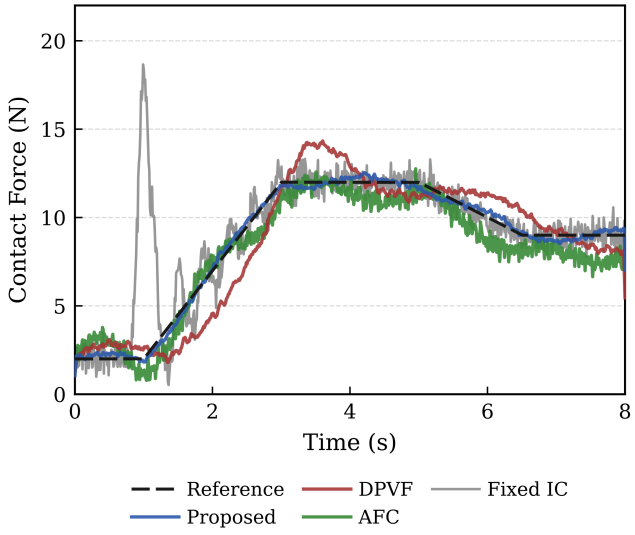


Figure 3. Force tracking comparison during a representative grasping trial on the three-phase smart meter [14,21].

The reference profile ramps from the initial contact force to the steady-state grip force. The proposed method tracks this reference with minimal overshoot. However, the fixed admittance controller produces a large impact peak at 18.6 N during the initial contact. Such peaks frequently damage the plastic housing. The proposed method suppresses this peak through the sigmoid force transition described. The initial value F_{init} is the preload force measured after the jaws establish firm contact, which is larger than the detection threshold. The reference decreases after $t \approx 5$ s because the object has reached the placement zone and the controller relaxes the grip force for release. The following Figure 4 visualizes the success rates for each equipment category.

The proposed method consistently outperforms all baselines. The margin is narrowest for the communication module. All methods exceed 85% on this lightweight and regular object. The margin widens significantly for the low-voltage current transformer. The heavy mass and irregular resin surface challenge the fixed-parameter baselines. The proposed adaptive stiffness and dynamic force compensation directly address these challenges. The proposed method shows relatively tight error bars. This consistency stems from the closed-loop learning architecture. The baselines exhibit larger variations. Their performance depends heavily on the initial object pose and the local surface geometry.

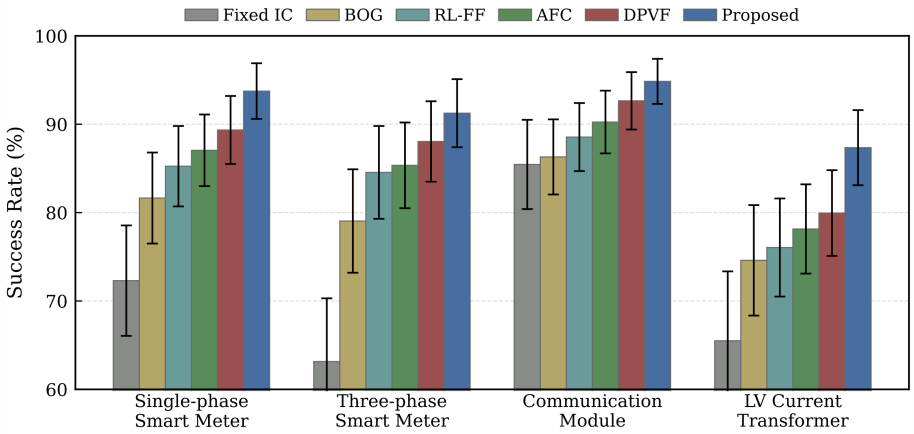


Figure 4. Grasp success rates across four equipment categories [2,12,14,21].

To separate the contributions of the adaptive impedance law and the reinforcement learning correction, two degraded variants of the proposed method were evaluated under the same protocol. The first variant disables the learning module and relies solely on the parameters generated in Section 2. The second variant applies the policy corrections to a fixed impedance baseline. The results are summarized in Table 3. The adaptive impedance law accounts for the larger share of the improvement, because it resolves the fundamental mismatch between fixed parameters and objects of divergent mass and stiffness. The learning correction provides a complementary refinement, which is most pronounced for the low-voltage current transformers, where contact transients are the most severe.

Table 3. Ablation study on the two main components.

Variant	Success Rate (%)	Damage Rate (%)
Fixed IC	71.6 ± 6.3	8.4 ± 3.1
RL correction only	83.8 ± 4.2	5.0 ± 2.2
Adaptive impedance only	86.3 ± 3.9	4.4 ± 2.0
Full method	91.8 ± 3.2	2.8 ± 1.4

A sensitivity analysis was conducted to evaluate the impact of the manually selected coefficients on the overall performance. The static friction coefficient, the dynamic load

factor, the baseline stiffness, the damping ratio in, and the transition rate were perturbed by ±20% around their nominal values, one parameter at a time. The results are reported in Table 4. The perturbation directions are consistent with physical intuition: a lower friction coefficient or a stiffer baseline leads to larger gripping forces and slightly higher damage, while an underdamped setting degrades both metrics. The nominal column reports the same reference configuration for all parameters, since one parameter is perturbed at a time.

Table 4. Sensitivity analysis under ±20% parameter perturbation.

Parameter	−20% (Success/Damage, %)	Nominal (Success/Damage, %)	+20% (Success/Damage, %)
μ_s	91.3/3.8	91.8/2.8	90.0/2.5
k_a	90.0/3.8	91.8/2.8	91.3/2.5
$K_{0,i}$	90.0/2.5	91.8/2.8	91.3/3.8
ζ_i	90.0/3.8	91.8/2.8	91.3/2.5
τ	91.3/2.5	91.8/2.8	90.0/3.8

Additional trials were performed to examine the robustness of the perception pipeline under challenging lighting. Additional trials per category were conducted at 150 lux and under approximately 1200 lux lateral glare. The results are reported in Table 5. Under strong glare, the depth stream degrades and the visual confidence coefficients decrease automatically, so the property fusion shifts its trust toward the database entries and the force feedback. The success rate decreases moderately from 91.8% to 87.5%, and no unsafe contact behavior was observed, because the force-based safety mechanisms remain effective regardless of the visual quality.

Table 5. Grasping performance under different lighting conditions.

Lighting Condition	Success Rate (%)	Damage Rate (%)
Normal, 500 lux	91.8 ± 3.2	2.8 ± 1.4
Dim, 150 lux	90.0 ± 3.6	2.5 ± 1.6
Lateral glare, 1200 lux	87.5 ± 4.1	5.0 ± 2.0

Several limitations of the proposed method should be noted. First, the property estimation module relies on a pre-established equipment database, and its accuracy may degrade when previously unseen object variants appear. Second, the material safety bound is derived from a linear stiffness model, which is an approximation that holds only within the small-deformation range of the tested objects. For objects with pronounced viscoelasticity, the residual model error is compensated online by the learning correction, while the projection bounds and the safety override prevent the contact force from exceeding the crushing limit. Nonlinear contact models of the Hunt–Crossley type will be considered in future work. Third, the visual perception layer degrades under extreme lighting, although the confidence-weighted fusion mitigates this effect. Fourth, the current validation is limited to a single robotic station, and the behavior in a multi-robot warehouse setting remains to be investigated.

6. Conclusions

This paper addresses the challenge of robotic grasping for fragile and heterogeneous power metering equipment. A multifunctional end-effector controller integrates compliant grasping algorithms with dynamic parameter adaptation. The controller estimates object properties and generates tailored impedance settings and force profiles. An online optimization mechanism based on deep reinforcement learning processes multi-

modal sensory feedback. A closed-loop framework coordinates visual perception with force-controlled execution.

However, the compliant grasping algorithm relies on a pre-established equipment database. When previously unseen object variants appear, the confidence-weighted fusion may deviate. In the future, an online learning module will be developed to update the property database incrementally. New object instances encountered during routine warehouse operations will be registered automatically. This capability reduces the dependency on pre-existing catalogs. The reinforcement learning pipeline will incorporate meta-learning strategies.

Author Contributions: Conceptualization, L.W. and C.W.; methodology, L.W.; software, D.Z. and Y.X.; validation, L.W., D.Z. and L.X.; formal analysis, C.W.; investigation, L.W. and Y.X.; resources, Y.X. and L.X.; data curation, D.Z.; writing—original draft preparation, L.W.; writing—review and editing, C.W. and K.G.; visualization, D.Z.; supervision, C.W. and K.G.; project administration, C.W.; funding acquisition, C.W. All authors have read and agreed to the published version of the manuscript.

Funding: This work was supported by the Technology Project of XJ Electric corporation (Research and System Development of Intelligent AI Robot Technology for the Metering Warehouse of Power Supply Stations), No. 2025G161.

Data Availability Statement: The original contributions presented in this study are included in the article. Further inquiries can be directed to the corresponding authors.

Acknowledgments: We would like to express our sincere gratitude to the reviewers for their professional opinions and valuable suggestions and our heartfelt thanks to the editorial board of the journal for their efficient work in supporting the rigorous presentation of the scholarly results. We would like to pay tribute to the academic community.

Conflicts of Interest: Authors Li Wang, Chaofan Wang, Dongyang Zhang and Yongxu Xing were employed by XJ Metering Co., Ltd. Author Linlin Xie was employed by XJ Electric Corporation. The authors declare that this study received funding from XJ Electric Corporation. The funder was not involved in the study design, collection, analysis, interpretation of data, the writing of this article or the decision to submit it for publication. The remaining authors declare that the research was conducted in the absence of any commercial or financial relationships that could be construed as a potential conflict of interest.

References

1. Phodapol, S.; Harnkhamen, A.; Asawalertsak, N.; Gorb, S.N.; Manoonpong, P. Insect Tarsus-Inspired Compliant Robotic Gripper with Soft Adhesive Pads for Versatile and Stable Object Grasping. *IEEE Robot. Autom. Lett.* **2023**, *8*, 2486–2493. [CrossRef]
2. Lechuz-Sierra, J.G.; Martin, A.E.H.; Sundaram, A.M.; Martinez-Cantin, R.; Roa, M.A. Bayesian Optimization for Robust Robotic Grasping Using a Sensorized Compliant Hand. *IEEE Robot. Autom. Lett.* **2024**, *9*, 10503–10510. [CrossRef]
3. Wang, W.; Cao, Y.; Li, Y.; Li, Z. A Modal Dissipating Energy Flow Analysis Method for Identifying the Hybrid Oscillation Sources in Power Systems. *IEEE Trans. Power Syst.* **2025**, *40*, 5503–5506. [CrossRef]
4. Jiang, Y.; Lin, C.; Wu, G.; Wu, W. Low-carbon scheduling for integrated electricity-hydrogen-gas systems with coordinated line-pack and tank-truck effects. *Appl. Energy* **2026**, *424*, 128468. [CrossRef]
5. Shi, X.; Guo, D.; Wang, W.; Cao, Y.; Shi, M.; Li, Y.; Zhou, L. Physical-Informed Detailed Aggregation of Wind Farm Based on Symbolic Regression: Structure, Solution and Generalizability. *IEEE Trans. Sustain. Energy* **2025**, *17*, 1511–1524.
6. Shen, Y.; Zhang, S.; Zhang, H.; Lu, Y.; Li, H.; Zhang, X.; Kecskemethy, A.; Zhu, B. Magnetic Robot with Bistable Compliant Mechanism for Snap-Though Jumping and Grasping. *IEEE Robot. Autom. Lett.* **2025**, *10*, 10822–10829. [CrossRef]
7. Pan, Z.; Wu, T.; Xie, K.; Zhao, T. Nodal Frequency Nadir Chance-Constrained Economic Dispatch Considering Contingency Frequency Service from Hydrogen Electrolysis. *IEEE Trans. Smart Grid* **2026**. [CrossRef]
8. Yu, J.; Zhao, J.; Zhong, J.; Lin, Z.; Xu, Y.; Peng, Y.; Cai, Y.; Cao, L.; Zhang, M.; Cao, Y. Towards fairness and low-carbon operation of energy hub: A multi-objective optimization framework with energy–carbon bidirectional coupling and heterogeneous uncertainties. *Appl. Energy* **2026**, *409*, 127475. [CrossRef]
9. Michikawa, R.; Endo, T.; Matsuno, F. A Multi-DoF Exoskeleton Haptic Device for the Grasping of a Compliant Object Adapting to a User's Motion Using Jamming Transitions. *IEEE Trans. Robot.* **2023**, *39*, 373–385. [CrossRef]

10. Liu, C.-H.; Yang, S.-Y.; Shih, Y.-C. Optimal Design of a Highly Self-Adaptive Gripper with Multi-Phalange Compliant Fingers for Grasping Irregularly Shaped Objects. *IEEE Robot. Autom. Lett.* **2023**, *8*, 7026–7033. [CrossRef]
11. Dai, W.; Xu, J.; Goh, H.H.; Shi, T.; Zeng, Z. Small Signal Equivalent Modeling for Large ES-Embedded DFIG Wind Farm with Dynamic Frequency Response. *IEEE Trans. Power Syst.* **2025**, *40*, 2324–2335. [CrossRef]
12. Jiang, Y.; Lin, C.; Li, B.; Zhang, J.; Wang, B.; Wu, W. Flexible interaction of integrated electricity-hydrogen-gas systems incorporating green hydrogen supply chain with varying operating characteristics. *Appl. Energy* **2026**, *422*, 128277. [CrossRef]
13. Dai, W.; Li, D.; Liu, H.; Liu, Y. A Cost Surrogate Model for TSO-DSO Coordination based on Polynomial Chaos Expansion. *IEEE Trans. Power Syst.* **2025**, *40*, 3580–3583. [CrossRef]
14. Zeng, C.; Li, S.; Chen, Z.; Yang, C.; Sun, F.; Zhang, J. Multifingered Robot Hand Compliant Manipulation Based on Vision-Based Demonstration and Adaptive Force Control. *IEEE Trans. Neural Netw. Learn. Syst.* **2023**, *34*, 5452–5463. [CrossRef] [PubMed]
15. D'Avella, S.; Sundaram, A.M.; Friedl, W.; Tripicchio, P.; Roa, M.A. Multimodal Grasp Planner for Hybrid Grippers in Cluttered Scenes. *IEEE Robot. Autom. Lett.* **2023**, *8*, 2030–2037. [CrossRef]
16. Dai, W.; Li, H.; Liu, H.; Goh, H.H.; Yuan, X.; Liu, Y.; Chen, B. An Efficient Affine Arithmetic-Based Optimal Dispatch Method for Active Distribution Networks with Uncertainties of Electric Vehicles. *IEEE Trans. Sustain. Energy* **2025**, *16*, 1021–1036. [CrossRef]
17. Sun, Y.; Lueth, T.C. Safe Manipulation in Robotic Surgery Using Compliant Constant-Force Mechanism. *IEEE Trans. Med. Robot. Bionics* **2023**, *5*, 486–495. [CrossRef]
18. Buzzatto, J.; Jiang, H.; Liang, J.; Busby, B.; Lynch, A.; Godoy, R.V.; Matsunaga, S.; Haraguchi, R.; Mariyama, T.; MacDonald, B.A.; et al. Multi-Layer, Sensorized Kirigami Grippers for Delicate Yet Robust Robot Grasping and Single-Grasp Object Identification. *IEEE Access* **2024**, *12*, 115994–116012. [CrossRef]
19. Zuo, K.; Yang, S.; Chua, Z. A Model-based Visual Contact Localization and Force Sensing System for Compliant Robotic Grippers. *IEEE Robot. Autom. Lett.* **2026**, *11*, 7788–7795. [CrossRef]
20. Li, T.T.; Zhao, A.P.; Wang, Y.; Li, S.; Fei, J.; Wang, Z.; Xiang, Y. Integrating solar-powered electric vehicles into sustainable energy systems. *Nat. Rev. Electr. Eng.* **2025**, *2*, 467–479. [CrossRef]
21. Kang, J.H.; Joshi, S.; Huang, R.; Gupta, S.K. Robotic Compliant Object Prying Using Diffusion Policy Guided by Vision and Force Observations. *IEEE Robot. Autom. Lett.* **2025**, *10*, 5505–5512. [CrossRef]
22. Thomasson, R.; Bernardini, A.; Li, H.; Xing, C.; Hajj-Ahmad, A.; Cutkosky, M. SLIM: A Symmetric, Low-Inertia Manipulator for Constrained, Contact-Rich Spaces. *IEEE Robot. Autom. Lett.* **2025**, *10*, 8682–8689. [CrossRef]
23. Tao, R.; Ma, Y.; Fan, J.; Fu, Y.; Jing, F.; Tan, M. Grasping-Based Robotic Threaded Assembly for Nonstandard Objects Under Uncertainty. *IEEE/ASME Trans. Mechatron.* **2026**, *31*, 603–615. [CrossRef]
24. Zhao, A.P.; Li, S.; Xie, D.; Wang, Y.; Li, Z.; Hu, P.J.-H.; Zhang, Q. Hydrogen as the nexus of future sustainable transport and energy systems. *Nat. Rev. Electr. Eng.* **2025**, *2*, 447–466. [CrossRef]
25. Liang, S.; Guan, Y.; Xu, J.; Qian, H.; Zhang, X.; Wu, D.; Ding, W.; Chen, R. AllTact Fin Ray: A Compliant Robot Gripper with Omni-Directional Tactile Sensing. *IEEE Trans. Autom. Sci. Eng.* **2025**, *22*, 19801–19813. [CrossRef]
26. Li, B.; Liu, Z.; Huang, H.; Zhong, H.; Li, Z.; Kang, W.; Guerrero, J.M. Two-Stage Risk-Based Scheduling for Electricity-Biogas Rural Microgrids with Biomass Fermentation. *IEEE Trans. Smart Grid.* **2026**. [CrossRef]
27. Jiang, L.; Tian, X.; Zhan, Q.; Xu, Q.; Zhang, Y. Impedance Control of an Anthropomorphic Hands without Finger Force Sensors. *IEEE Trans. Autom. Sci. Eng.* **2024**, *21*, 5779–5789. [CrossRef]
28. Ilyushin, Y.; Pervukhin, D.; Afanasieva, O.; Klavdiev, A.; Kolesnichenko, S. The Methods of the Synthesis of the Nonlinear Regulators for the Distributed One-Dimension Control Objects. *Mod. Appl. Sci.* **2015**, *9*, 42–61. [CrossRef]

Disclaimer/Publisher's Note: The statements, opinions and data contained in all publications are solely those of the individual author(s) and contributor(s) and not of MDPI and/or the editor(s). MDPI and/or the editor(s) disclaim responsibility for any injury to people or property resulting from any ideas, methods, instructions or products referred to in the content.